Solar light-driven simultaneous pharmaceutical pollutant degradation and green hydrogen production using a mesoporous nanoscale WO$_3$/BiVO$_4$ heterostructure photoanode

Katherine Rebecca Davies [a], Michael G. Allan [b], Sanjay Nagarajan [c], Rachel Townsend [d], Tom Dunlop [a], James D. McGettrick [a], Vijay Shankar Asokan [e,1], Sengeni Ananthraj [f], Trystan Watson [a], A. Ruth Godfrey [d], James R. Durrant [a,g], M. Mercedes Maroto-Valer [h], Moritz F. Kuehnel [b,i], Sudhagar Pitchaimuthu [a,h,*]

[a] *SPECIFIC, Faculty of Science and Engineering, Swansea University, Swansea, Wales, UK*
[b] *Department of Chemistry, Faculty of Science and Engineering, Swansea University, Singleton Park, SA2 8PP Swansea, Wales, UK*
[c] *Department of Chemical Engineering, University of Bath, Bath BA2 7AY, UK*
[d] *Swansea University Medical School, Faculty of Medicine, Health and Life Science, Singleton Park, Swansea University, SA2 8PP, U.K.*
[e] *Environmental Inorganic Chemistry, Department of Chemistry and Chemical Engineering, Chalmers University of Technology, S-412 96, Göteborg, Sweden*
[f] *Department of Applied Chemistry, School of Advanced Science and Engineering, Waseda University, 3–4-1 Okubo, Shinjuku-ku, Tokyo, Japan*
[g] *Department of Chemistry and Centre for Processable Electronics, Imperial College London, London, UK*
[h] *Research Centre for Carbon Solutions (RCCS), Institute of Mechanical, Processing and Energy Engineering, School of Engineering and Physical Sciences, Heriot-Watt University, Edinburgh, UK*
[i] *Fraunhofer Institute for Wind Energy Systems IWES, Am Haupttor 4310, 06237 Leuna, Germany*

ARTICLE INFO

ABSTRACT

Photoelectrocatalysis is one of the most favourable techniques that could be used in this remit as it has the potential to utilise natural sunlight to generate oxidants in situ to mediate effective pollutant degradation. This work, therefore, utilises a mesoporous nanoscale WO$_3$/BiVO$_4$ heterostructure photoanode to effectively degrade ibuprofen in wastewater combined with simultaneous green hydrogen generation at the cathode under simulated sunlight. A near complete degradation (>96%) of ibuprofen (starting concentration of 100 mg/L), with no hazardous intermediates (determined via mass spectrometry analysis), along with simultaneous H$_2$ evolution of 114 μmol/cm^2 after 145 min was demonstrated in this work. In addition, intermediate product analysis, the role of the type of in situ oxidants on degradation, the mechanistic pathway of degradation, and the material characteristics of mesoporous photoanode were also investigated. First experimental evidence of in situ generated H$_2$O$_2$ contributing to the degradation of ibuprofen is presented.

1. Introduction

Pharmaceutical drug consumption in the healthcare sector has increased continuously in the last two decades. It has resulted in approximately 4000 active pharmaceutical ingredients being issued worldwide in 2018 [1]. Active pharmaceutical ingredients (APIs) are an increasing pollution threat to our freshwater sources due to ineffective wastewater (WW) treatment processes and its subsequent release into the environment [2]. APIs have been detected in ng/L to mg/L ranges within drinking water and freshwater sources worldwide [3]. Mainly,

these APIs induce negative health effects on aquatic life and humans via antibiotic resistance, cause acute and chronic damage [4], behavioural changes, a build-up in tissue [5], issues with reproductive systems [6] and inhibition of cell production [7] even at low ng/L concentrations [1]. Therefore, the severity of pharmaceutical drug pollutants in water streams have been examined by several researchers [2, 8–10].

One of the most concerning pharmaceutical compounds in the water environment is ibuprofen (IBP), due to it being the third most consumed drug [11]. This has resulted in a high concentration of IBP reaching our WW treatment plants. For instance, ~8600 ng/L IBP have been observed

at Canadian wastewater treatment plants [12]. Due to the recalcitrant structure of IBP, it is extremely difficult to degrade the compound and mineralise it completely before environmental discharge from conventional WW treatment plants [13]. This has resulted in IBP reaching freshwater sources which is a significant concern given IBP has been reported to cause endocrine disruption in *Mytilus galloprovincialis* [14], oxidative stress and membrane damage within the digestive gland, and an increase in lipid peroxidation levels in mussels [15]. Whilst, Lange et al [16]. showed that IBP concentrations between 10 and 100 ng/L can decrease the behavioural response of amphipod crustaceans *Gammarus pluex*. A 21-day LC50 (lethal concentration sufficient to kill 50% of the population) concentration of IBP for *Daphnia magna,* a brackish and fresh water planktonic crustacean was found to be ~4 mg/L [17]. So, it is imperative to remove even lower concentrations of IBP present in water. This implies the elimination of IBP from wastewater is crucial. Therefore, finding an alternative, sustainable technology that can completely remove IBP from WW is essential to reduce its environmental impact.

Typically, recalcitrant pollutants in WW are mineralised using advanced oxidation processes due to their ability to generate highly oxidising species in-situ. Photo-electrocatalysis (PEC) is one such advanced oxidation process that is of emerging interest to decontaminate WW. Particularly, PEC has been successfully exploited previously to degrade a range of pollutants into non-toxic products completely [18–22]. PEC works by utilising a photoanode containing a light-responsive semiconductor catalyst coated onto a conductive substrate (glass, steel, etc.) with a counter electrode and reference electrode [23]. The WW acts as a source of electrolytes and source of electron are placed in the cell hosting the photoanode and cathode. When a light source irradiates the semiconductor photoanode, it allows photons with the equivalent or higher energy than the bandgap to be absorbed. It causes the electrons to move from the valance band to the conduction band. This results in holes left in the valance band, which oxidise water molecules and generate protons (H^+) as a by-product. In PEC techniques, a small applied electric potential, typically 0.1 – 1.0 V vs. NHE (normal hydrogen electrode) is required to create a band bending effect in the semiconductor-electrolyte interface, which drives the photoelectrons from the semiconductor surface to the charge collector [24]. These photoelectrons transport to the counter electrode, reducing the protons to generate hydrogen gas.

Recovering hydrogen (H_2) gas via PEC or photocatalysis mediated pollutant degradation process is an innovative approach [25–27]. Conventional hydrogen production processes, such as steam methane reforming, is carbon intensive, with 9–12 kg CO_2/kg H_2 produced [28]. Contemporary 'green' water electrolysis processes are therefore favourable with < 0.6 kg CO_2/kg H_2 produced [28–30]. The problem however is the requirement of fresh water for electrolysis leading to a large freshwater footprint of 9 kg freshwater/kg hydrogen produced [31]. On the contrary, when WW is used in a tandem process for its simultaneous treatment coupled with hydrogen generation, the process will truly be green. In the case of PEC based tandem processes, the pollutant in WW acts as a sacrificial electron donor leading to its degradation coupled with the reduction of protons at the cathode for hydrogen generation [32]. Such a process is expected to reduce the levelised cost of hydrogen (LCOH) [25]. The work presented in this manuscript is an attempt towards achieving this and has duly demonstrated the PEC of simulated IBP WW for its degradation coupled with H_2 generation. The main challenges with PEC based systems however lie in the complexity of electrode fabrication without sacrificing the electronic conductivity of the materials, and the thickness-dependent photocharge carrier recombination which is also addressed here [33].

Visible light-driven semiconductor photoanodes such as WO3, BiVO4, C3N4, CdS, Ta3N5, and bismuth oxyhalides have shown effective pollutant degradation performance compared to commercially available TiO2 [20, 34–38]. It is beneficial to move away from UV activated photoanodes but towards visible light activated narrow bandgap energy

materials (2.2–2.8 eV) to effectively harness sunlight and maximise the photonic efficiency [39]. However, the charge recombination behaviour at a single semiconductor catalyst limits the overall performance of the water pollutant degradation. Hetero-structured semiconductors promote charge separation (e- and h+) via type-II junction formation and can overcome charge recombination at electrode/electrolyte interfaces [40,41]. In this context, nanoscale WO3/BiVO4 is a benchmark photoanode configuration in water splitting hydrogen generation due to its (a) effective charge separation at low applied potential energy, (b) extended visible light absorption, thus exhibiting significant photocurrent density (2–6 mA cm^{-2}) in a PEC cell [42–46]. The higher photocurrent density generation at WO3/BiVO4 photoanode compared to the respective individual semiconductor photoanode indicates the merits of heterostructure photoanodes in PEC [47]. Usually, the photocurrent density of the WO3/BiVO4 photoanode can be improved by co-catalyst deposition, electrolyte pH modification, and passivation layer coatings [48–50]. A conventional flat type WO3/BiVO4 is appropriate for splitting water into oxygen and hydrogen generation, but for WW treatment applications, it limits the pollutant mass transport on the electrode surface [51]. It is anticipated that mesoporous WO3/BiVO4 photoanodes can enhance the water pollutants' percolation, which enhances mass transfer for efficient pollutant degradation [52–54].

This work demonstrates the feasibility of mesoporous type nanoscale WO3/BiVO4 heterostructure photoanode (Scheme 1a) in simultaneous IBP degradation at photoanode and hydrogen gas evolution at the cathode compartment. The mesoporous channels at WO3/BiVO4 will offer high mass transport of the electrolyte, which is anticipated to result in high interfacial contact between IBP and the catalyst surface. The schematic illustration of simultaneous IBP degradation at the anode compartment and hydrogen gas generation at the cathode compartment is shown in Scheme 1b.

Current literature exploring PEC for IBP degradation are limited and have only presented incremental research findings mainly focussing on material development or enhancing the degradation efficiencies of IBP [55–59]. A gap still exists in the area of degradation pathway identification from a chemistry and environmental fate viewpoint and improving technology readiness from the engineering viewpoint. This work addresses one of these aspects i.e., PEC mediated IBP degradation pathway identification. It is critical to address this as in most cases, the degradation of a recalcitrant parent compound leads to the formation of more toxic by-products [60]. Elucidating the pathway presents venues to intensify the degradation towards non-toxic safe WW discharge. In addition to addressing a specific challenge with IBP degradation, this work also demonstrates a novel simultaneous green hydrogen production route that has the potential to decarbonise the WW industry and accelerate net zero transition.

The aim of this work is to primarily demonstrate the capability of a mesoporous type nanoscale WO3/BiVO4 heterostructure photoanode for IBP degradation coupled with simultaneous hydrogen evolution in a PEC cell. During the course, crucial processing parameters, such as the influence of ionic salt in the electrolyte and its concentration on IBP degradation as well as hydrogen evolution were examined. Intermediate product analysis, role of the type of in situ oxidants on degradation, mechanistic pathway of IBP degradation, and the material characteristics of mesoporous photoanode were also investigated in this work.

2. Experimental

2.1. Preparation of mesoporous WO3/BiVO4 photoanode

All the chemicals were received from Sigma Aldrich unless stated otherwise. In the first step, a homogenous WO3 paste was prepared using commercial WO3 nanocrystalline powder (100 nm size). We adopted Regan's protocol where WO3 nanopowder was utilised instead of TiO2 [61]. Briefly, the preparation involved the following stages, (a) grinding 5 g of WO3 with 1 mL of acetic acid for 5 min using mortar and pestle,
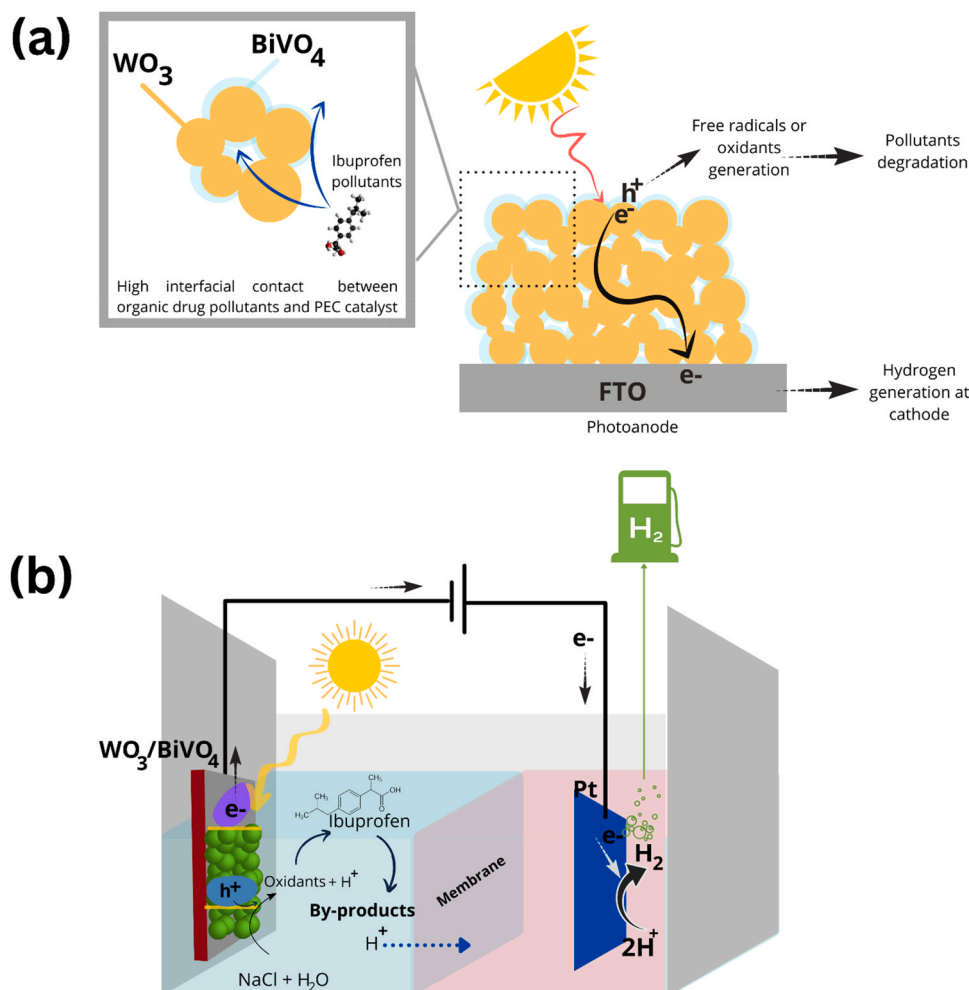
Scheme 1. (a) Schematic structure of mesoporous type WO$_3$/BiVO$_4$ photoanode for solar light-driven PEC water pollutants degradation. (b) Schematic illustration of simultaneous IBP pollutants degradation (anode) and green hydrogen generation (cathode) at WO$_3$/BiVO$_4$ photoanode based dual compartment PEC cell. FTO-fluorinated tin oxide.

(b) adding 1 mL of deionised water and grinding for 1 min (repeat this 6 times), (c) adding 1 mL of ethanol and grinding for 1 min (repeat this 15 times), (d) adding 2.5 mL of ethanol and grinding for 1 min (repeat 6 times). Then, the WO$_3$ colloid was transferred into a closed beaker using 100 mL of ethanol. The solution was then magnetically stirred (150 RPM) for 1 min, sonicated for 10 min (10 s on/off) and magnetically stirred (150 RPM) for 1 min again. Then 20 g of α-terpineol was added to the above colloidal solution, and then it was magnetically stirred for 1 min, sonicated for 10 min (10 s on/off) and magnetically stirred for 1 min again. Once this step was completed, then 30 g of 10% (w/w) ethyl cellulose in ethanol was added, and the solution was magnetically stirred for 1 min, sonicated for 10 min (10 s on/off), and magnetically stirred for 1 min again. The final step used a rotary evaporator to remove the ethanol from the paste. The setting was under vacuum, and the temperature ranged from 50° to 70°C, the speed of rotation was 90 – 120 RPM, and it was conducted for 1 h. Once the homogenous WO$_3$ paste was ready, it was applied on the pre-cleaned fluorine-doped tin oxide coated (FTO) glass (Pilkington 12 Ω sheet resistance) by utilising the doctor blade method. A hotplate was utilised to anneal the samples by utilising the following conditions: (a) Ramp Time = 1 h, (b) Set temperature = 450 °C and (c) Annealing Time = 3 h. This step was repeated twice to make a 2-layer WO$_3$ on the FTO glass.

The BiVO$_4$ solution was prepared by utilising the method reported by Choi et al [42]. This was done by mixing 0.1462 g of ammonium metavanadate, 0.6061 g of bismuth nitrate pentahydrate, 0.4803 g of citric acid, 0.825 g of nitric acid and 2.9 mL of deionised water together. The solution was then sonicated for 10 min. Once the solution was finished, it was spin-coated on top of the WO$_3$ surface by utilising a spin coater with a setting of 500 RPM for 5 s and 2000 RPM for 40 s. The WO$_3$/BiVO$_4$ photoanode was annealed using the following settings on an enclosed hotplate: (a) Ramp Time = 2.5 h, (b) Set Temperature = 500 °C and (c) Annealing Time = 1 h. Finally, an insulated copper wire was attached to the uncoated area of WO$_3$/BiVO$_4$ coating on FTO glass, and the electrode was insulated to avoid the electrolyte interaction using epoxy resin glue. The active area of the electrode was approximately 1 cm^2.

2.2. Characterisation

The X-ray diffraction measurements were conducted utilising a Bruker D8 Discover X-ray Diffractometer with a copper source (40 kV, 40 mA) and a 1D detector in Bragg-Brentano. The X-photoelectron spectroscopy (XPS) measurements were achieved by utilising a Kratos Axis Supra using a monochromatic Al Kα X-ray source operated at 225 W (15 mA emission current). The experimental data was deconvoluted with Fourier transform and fitted with CasaXPS software. The scanning electron microscopy (SEM) images were captured using a JEOL 7800 F FEG-SEM with an Oxford Instrument X-MaxN Energy Dispersion Spectra (EDS) Detector with a 50 mm^2 window. The high resolution-transmission electron microscopy (HR-TEM) image was captured using

a FEI Technai F2O system. The UV–vis diffuse reflectance spectra (UV-Vis DRS) were obtained using a Perkin Elmer Lambda 365 system.

2.3. Photoelectrocatalysis experiments

PEC experiments were demonstrated using a two-compartment cell with a proton exchange membrane (Nafion™ 117) separating the anodic and cathodic compartments. In the anodic compartment (50 mL capacity), the $WO_3/BiVO_4$ photoanode working electrode and Ag/AgCl reference electrode were immersed in a 0.5 M NaCl electrolyte. At the same time, the cathodic compartment had conventional platinum (Pt) wire as a counter electrode. For the chronoamperometry experiments, a Zahner potentiostat (Thales Zahner Zennnium) was utilised, with an applied potential of 1.2 V (vs. Ag/AgCl) to the $WO_3/BiVO_4$ working electrode and a 30 s off/on chopped light of 1 Sun solar light (Solar Simulator 350 – 1800 nm, HAL-320 W, Asahi Spectra) for 5 min. The linear sweep voltammetry experiments were conducted by using a Zahner potentiostat (Thales Zahner Zennnium) with an applied potential range from – 0.5–1.5 V (vs. Ag/AgCl) and carried out in the dark and 1 Sun condition (Solar Simulator 350 – 1800 nm, HAL-320 W, Asahi Spectra). All the experiments were repeated three times unless otherwise stated.

2.4. Ibuprofen degradation experiments

The IBP degradation was conducted in the PEC set-up as described above. However, the 0.5 M NaCl electrolyte in the anodic compartment was spiked to contain 100 µg/mL of IBP. The experiment was initially conducted with an applied potential of 0.6 V (vs. Ag/AgCl) for 30 min in the dark to allow absorption equilibrium, then placed under 1 Sun irradiation for 2 h. For the optimisation of the process, the applied potential was increased from 0.6 V to 1.5 V in 0.3 V intervals. Once the applied potential was optimised, the NaCl electrolyte concentration was increased to 1 M. The electrolyte samples (10 µL) were analysed using liquid chromatography system coupled with a UV detector (LC-UV) (Agilent 1200 LC-UV system with a Waters X-select C-18 column (2.1 mm × 100 mm)). The mobile phases were 0.1% formic acid in water and acetonitrile, which were pumped at 0.250 mL/minute using a gradient approach (75:25–0:100 over xx minutes, with a column wash at 100% B for XX minutes and recondition step for YY minutes). The UV detection wavelength was set at 265 nm, to target IBP. The final sample from the optimised IBP degradation experiment was analysed using the same LC settings as above but with a Waters Xevo TQ-S mass spectrometer, operating using electrospray ionisation in positive ion mode, at a capillary and cone voltage of 3.5 kV and 5 V, respectively, with a source temperature of 500 °C, and a desolvation and cone gas flowrate of 600 and 150 L/hr, respectively. Data was acquired over a mass range of 50–500 mass-to-charge (m/z) range, and used a collision induced dissociation (CID) energy of 30 eV for the tandem mass spectrometry work.

2.5. Hydrogen peroxide quantification

Quantofix H_2O_2 stripes were utilised to quantify the H_2O_2 being produced during the IBP degradation experiment. These stripes can only give an approximation with detection range between 0.5 and 25 mg/L; thus, the results have low precision for the H_2O_2 concentrations. The stripes were dipped into the electrolyte every 30 min and examined against the colour chart to obtain the H_2O_2 concentration.

2.6. PEC hydrogen generation experiments

H_2 generation experiments were conducted similar to IBP degradation experiments, except the cathodic compartment had an inlet and outlet line to and from a gas chromatography (GC) system. A PalmSens EmStat 3 + potentiostat was used. The PEC cell was irradiated with a

solar simulator (Thermo-Oriel) equipped with an AM 1.5 G filter (Newport) at 1 sun; experiments were performed in triplicate. A Shimadzu Nexis GC-2030 was used to quantify the hydrogen gas generated. It is configured with a barrier-discharge ionisation detector (BID) and a molecular sieve column with an internal diameter of 530 µm and a length of 30 m. The capillary column temperature was set to 140 °C with the BID set to 250 °C and Helium (BOC) was used as the carrier gas. The run time of the method was 5 min, programmed with an auto-injection after 2 min and a backflush at 2.29 min to avoid moisture from being injected into the column. The gas samples were carried from the PEC cell headspace by the purge gas (nitrogen, BOC) via a mass flow controller (Bronkhorst) to the GC sample loop (Restek, 2 mL). After 2 min flushing of the sample loop, the gas mixture (sample and purge gas) was periodically sampled using a split injection (5:1). 10-point calibration of the GC was done using a 2000 ppm H_2 in CO_2 standard (BOC) diluted with N_2 to 50–1000 ppm using a set of mass flow controllers. From the determined H_2 concentration in the purge gas and the purge gas flow rate, the H_2 evolution was calculated assuming constant H_2 production in between sampling points.

3. Results and discussion

3.1. Composition of the photoanode material

The crystalline structure of WO_3 and $WO_3/BiVO_4$ films were studied using an X-ray diffractometer (Fig. 1a). The diffraction peaks were observed at 23.1°, 23.6° and 24.3°, which corresponds to (002), (020) and (200) crystalline phases of WO_3. It indicates orthorhombic WO_3. A small crystalline peak at 18.5° in the $WO_3/BiVO_4$ sample (Fig. 1b) implies the (101) crystalline phase of $BiVO_4$ has been formed [62–65]. Further, the surface morphology of WO_3 and $WO_3/BiVO_4$ films were studied by FESEM and HR-TEM (Fig. S1 a-b, Fig. 1 c-f, respectively). Fig. 1 (c) shows the WO_3 particles were in an anisotropic shape and size between 50 and 120 nm. The high magnification image (Fig. 1d) displayed a lattice diameter of 0.26 nm corresponding to the (021) phase of WO_3. Fig. 1e shows the $BiVO_4$ thin film coating with a thickness of 10 nm well covered with WO_3 crystals. However, the (101) lattice planes of $BiVO_4$ as observed in XRD were not observed in the HR-TEM images (Fig. 1b). This might be due to the poor crystalline formation of $BiVO_4$, which is difficult to determine from the HR-TEM images. Another WO_3 lattice observed from $WO_3/BiVO_4$ sample (Fig. 1 f) showed 0.26 nm corresponds to (202) crystalline phase. The WO_3 crystalline phase observations are in line with XRD results.

The surface morphology of the $WO_3/BiVO_4$ photoanode was characterised by SEM and shown in Fig. S1 (a). The image shows that the photoanode has a nanoporous surface as the grain size varies from 60 to 350 nm. While the EDS analysis Fig. 1(b) shows the total coverage of $BiVO_4$ over WO_3. It implies that the spin coating of the $BiVO_4$ layer on top of WO_3 successfully created an effective heterojunction. It can be further verified with a HR-TEM image (Fig. 1e).

The chemical environment of WO_3 and $BiVO_4$ coating was examined with XPS to provide detailed information about metal ion diffusion (W or Bi) or oxygen vacancies (V_o) that could occur at the $WO_3/BiVO_4$ interface. From the literature for WO_3, the $W4f_{5/2}$ and $W4f_{7/2}$ associated with the target coordination state of W^{6+} are reported to have binding energies of 35.1–35.4 eV and 37.2–37.6 eV, respectively [64,66,67]. Fig. 2(a) shows strong peaks at 35.18, 35.55 eV, 37.29 and 37.66 eV for the fabricated films indicating that both WO_3 and $WO_3/BiVO_4$ photoanodes have been successfully manufactured to contain the target coordination state of W^{6+} [64,66].

However, a slight shift in the binding energies associated with W in $WO_3/BiVO_4$ photoanode was also observed. This difference in binding energy usually suggests a chemical shift has occurred, possibly due to a change in oxidation state of the atom or the physical environment, with a higher oxidation state of W in $WO_3/BiVO_4$ than in WO_3 films. Therefore, this data indicates that the $BiVO_4$ coating on the WO_3 layer alters

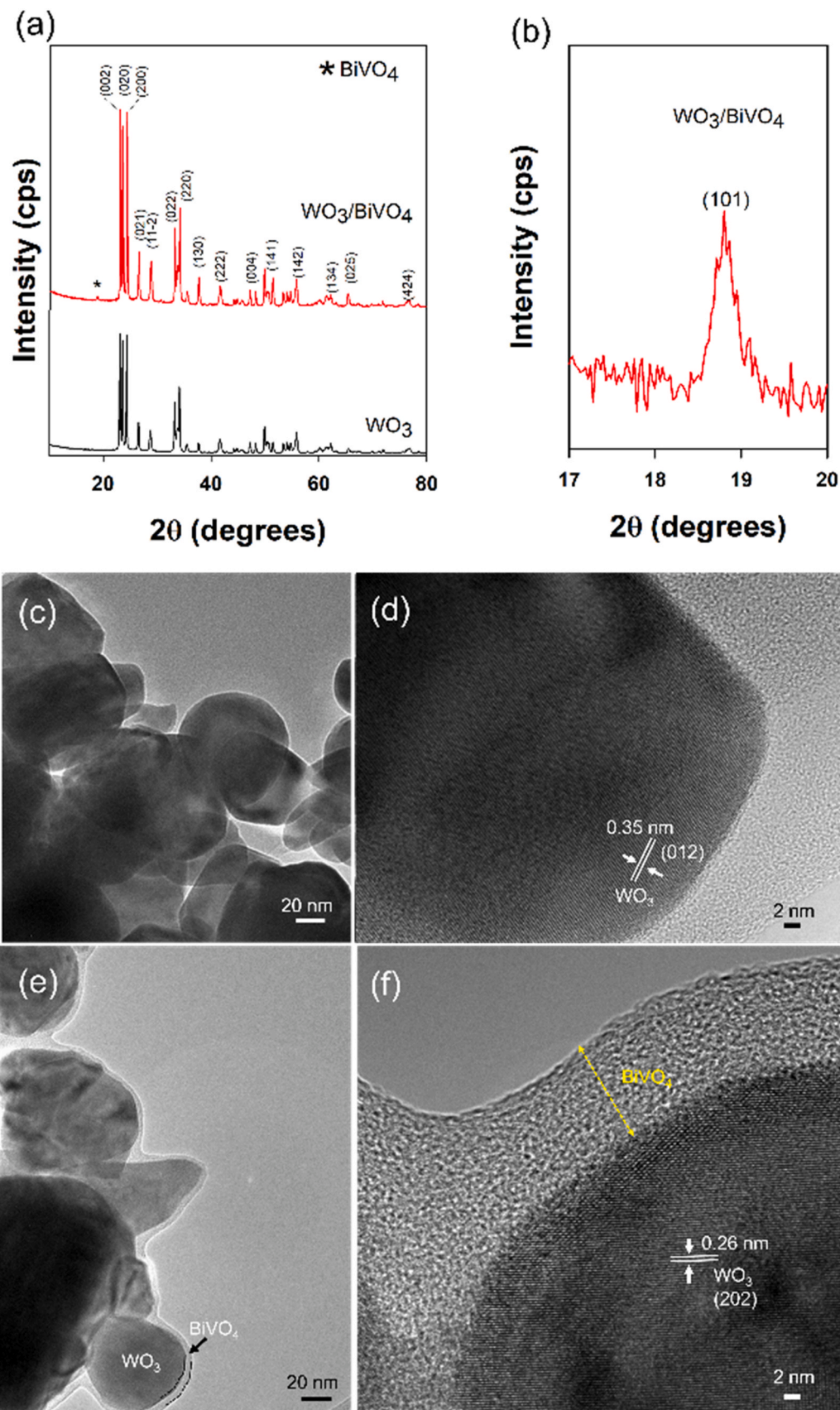**Fig. 1.** (a) X-ray diffraction patterns of WO₃ and WO₃/BiVO₄ films coated onto FTO substrate, (b) Magnified view of X-ray diffraction patterns observed from Fig. 1 (a) for clear eye guidance. HR-TEM images of WO₃ film at (c) 20 nm and (d) 2 nm. HR-TEM images of WO₃/BiVO₄ films at (e) 20 nm and (f) 2 nm.
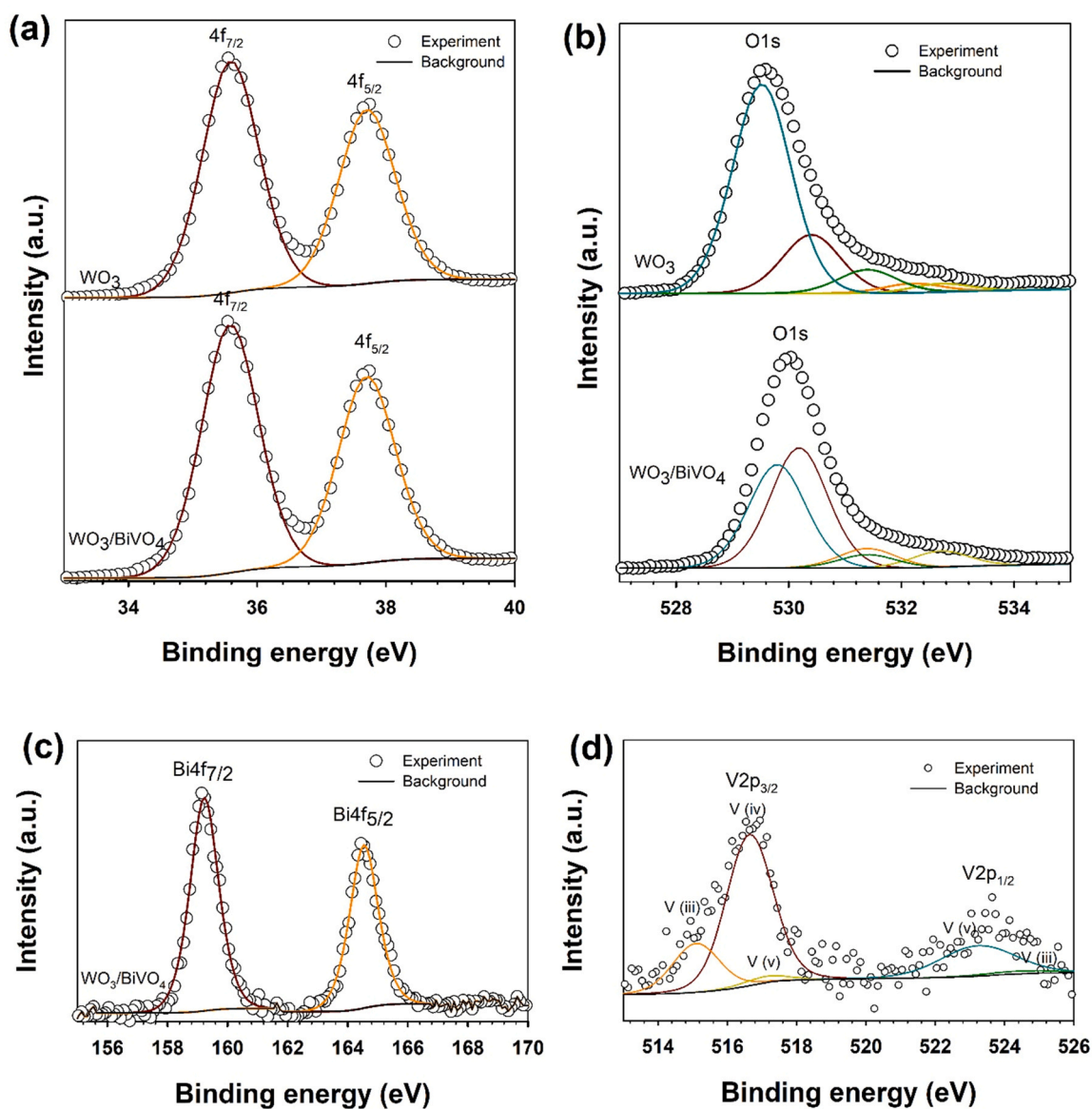
Fig. 2. XPS core spectra of (a) W4f and (b) O1s measured from WO_3 and $WO_3/BiVO4$ films. XPS core spectra of (c) Bi4f and (d) V2p measured from $WO_3/BiVO_4$ films. The circles represent experimental data, and solid lines denote the data fitting by CASA software.

the chemical environment and resulting binding energy. Further analysis of the XPS spectra in Fig. 2(b-d) also shows sound evidence for the formation of the target $BiVO_4$ coating. For example, multiple O1s peaks associated with lattice oxygen (529.6 and 530.4 eV) and surface hydroxyl groups (-OH) (531.5 eV) were observed, suggesting appropriate oxidation of the material. Whilst, peaks at 159.21 eV and 164.52 eV (Fig. 2(c)) indicative of $Bi4f_{7/2}$ and $Bi4f_{5/2}$, respectively [44], and at 516.5 eV and 524.1 eV (Fig. 2(d)) indicative of $V2p_{3/2}$ and $V2p_{5/2}$, respectively [64] strongly suggest that the target coordination states of Bi (3^+) and V (5^+) associated with $BiVO_4$, have been formed within the electrode coating.

3.2. Characterisation of the photoanode material in initiating oxidation

To explore if the $WO_3/BiVO_4$ photoanode can efficiently absorb visible light photons from the solar spectrum, optical absorption measurements were obtained. These results (Fig. 3) show that the visible light activity of WO_3 is extended from approximately 450 nm to 490 nm with $BiVO_4$ heterolayer deposition, and that the $WO_3/BiVO_4$ heterostructured film exhibits higher photo absorption than the original $BiVO_4$

film. The bandgap energy of the WO_3, $BiVO_4$ and $WO_3/BiVO_4$ films are estimated using Tauc plots using Kubelka-Munk (Fig. S3). The extrapolation of a straight line which intersects the X-axis provides the bandgap energy value. These straight lines indicated in Fig. S3 are indicated in red colour derived by straight line fitting process with 99.9% of accuracy. The estimated bandgap energy values of WO_3, $BiVO_4$ and $WO_3/BiVO_4$ are found to be 2.79, 2.66 and 2.65 eV, respectively. The $BiVO_4$ deposition onto WO_3 narrows the bandgap energy from 2.79 to 2.65 eV, indicating that the $WO_3/BiVO_4$ photoanode can efficiently absorb visible light photons for photocatalytic activity [45,68].

The potential for the $WO_3/BiVO_4$ photoanode to initiate the degradation of organic materials in water via oxidation was initially examined using water splitting reactions with an aqueous 0.5 M NaCl electrolyte (see Fig. S4). Earlier reports using NaCl-based electrolytes at this selected concentration showed that NaCl can effectively scavenge the photoholes from the valence band of $WO_3/BiVO_4$ heterostructured photoanode, due to high electrolyte conductivity, which helping to maintain the charge separation required for photocatalytic activity [69]. Chronoamperometry results of $WO_3/BiVO_4$ photoanode under dark and light irradiation conditions confirms this, with the absence of
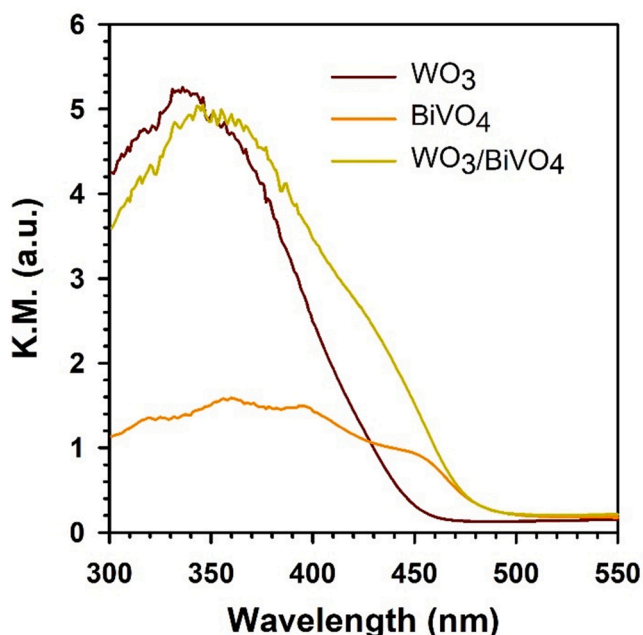
Fig. 3. (a) Optical absorption spectra (Kubelka-Munk) of WO_3, $BiVO_4$ and $WO_3/BiVO_4$ coatings onto FTO substrate.

photocurrent generation when no electrolyte is used (see Fig. 4). However, when NaCl is applied, the $WO_3/BiVO_4$ photoanode based PEC cells appear to offer a highly effective water oxidation system, with a high photocurrent density (3.4 mA.cm^{-2} at 2 V RHE) observed within the JV plots in Fig. S4. This, with the greater visible light activity and charge separation at the electrode/electrolyte interface, indicates that $WO_3/BiVO_4$ can provide a more effective water oxidation process in relation to the unmodified WO_3 photoanode material.

3.3. Optimisation of the photoanode material

To further enhance the photocurrent generation, the electrolyte composition to increase charge separation was investigated with the $WO_3/BiVO_4$ photoanode. Past work has shown a Na_2SO_4 electrolyte can be used with similar performance to NaCl with WO_3 photoanodes, and this was investigated to achieve optimum performance with this new $WO_3/BiVO_4$ photoanode material. In the case of a NaCl-based electrolyte, the photocurrent generation is steady in comparison to Na_2SO_4; for the latter, the photocurrent starts to decrease with time, suspected due to reduced photocharge carriers transfer at electrode/electrolyte interfaces [70]. Therefore, based on these results, NaCl was chosen as the appropriate electrolyte for supporting the degradation of IBP.
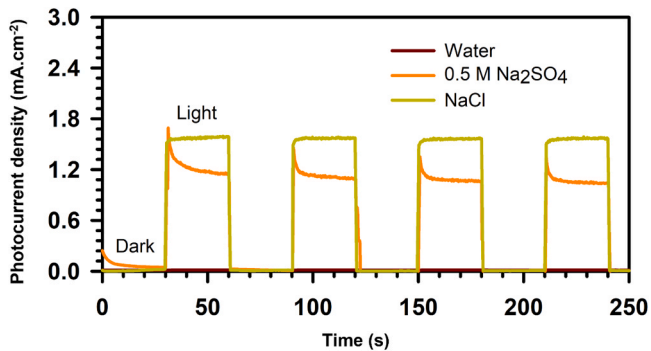

Fig. 4. Chronoamperometry plots of $WO_3/BiVO_4$ photoanodes in different electrolytes. Note that the experiments were measured at an applied potential 1.23 V RHE.

IBP degradation experiments were carried out with chronoamperometry mode under an applied potential of 1.15 V vs. RHE using 0.5 M NaCl electrolyte. The IBP removal from the water was quantified at dark and 1 Sun conditions using the LC-UV method, and the results are presented in Fig. 5 (a). Briefly, to successfully degrade IBP it is anticipated that the compound will first need to be adsorbed onto the $WO_3/BiVO_4$ surface, with the photoholes generated from the semiconductor catalyst initiating oxidation of IBP either directly on the surface of the material, or indirectly via the reactive oxygen species within the electrolyte. In terms of IBP degradation, differences were observed following the application of light, with increased IBP removal (27.9% to 52.3 $\pm$ 5%) in the presence of photons. With the reduced photocatalytic performance noted in absence of light (in above results), this lower percentage IBP removal was not unexpected, and the levels observed were suspected to be primarily due to the adsorption of IBP on $WO_3/BiVO_4$ surface rather than photocatalytic degradation. This was supported with the absence of intermediate IBP products during the dark conditions (Fig. S5) and confirms degradation will require both surface adsorption and photoelectrocatalysis [57, 71–72]. However, given the charge separation at $WO_3/BiVO_4$ interface (and anticipated photocatalytic performance) is dependent on the applied potential, percentage removal of IBP was evaluated at selected voltages (1.15 V, 1.45 V, 1.75 and 2.1 V vs. RHE). As shown in Fig. 5 (b), IBP degradation improves with increasing applied potential to 1.75 V vs. RHE, achieving a maximum IBP removal of 81.7 $\pm$ 4.5% after 150 min of reaction. However, when increased above 1.75 V vs. RHE no further increase in IBP degradation was observed, possibly due to the photoelectron generation being fixed at the photoanode under a constant 1 Sun irradiation.

The increment in the applied potential to the circuit enhances the band bending at the $WO_3/BiVO_4$/electrolyte interface, thus providing a higher driving force for the photoelectrons to move from the $BiVO_4$ surface to the charge collector via WO_3 [73]. Once the photoelectrons effectively separate from the semiconductor, the hole lifetime can be extended to enable effective pollutant degradation [74]. However, increasing the electric potential in the circuit above the flat band potential does not change the charge carrier collection. Instead, it initiates a competitive reaction on the photoanode surface. Secondly, at higher potentials, the by-products are formed at faster rates, which means there is higher competition for the active sites, thus reducing the ibuprofen degradation [75]. Thirdly, when the applied potential is at its optimum, the space charge layer is roughly the same thickness as the photoanode resulting in the complete separation of the charge carriers [76]. Consequently, increasing the applied potential beyond this point causes the space charge layer to relocate, which results in charge recombination and reduces the IBP degradation [76]. Finally, pushing the applied potential beyond the optimal amount causes oxygen generation, which competes with the ibuprofen degradation reaction, resulting in lower degradation rates [77].

In addition to the electrolyte type, the concentration and subsequent ionic conductivity of the electrolyte was also investigated to improve the charge separation at the electrode/electrolyte interface. Despite typical conditions in published works involving 0.5 M NaCl, it is anticipated that an increase in the electrolyte (salt) concentration would result in an increase in ionic transport from the solution to the electrodes, further driving charge separation and degradation. By changing the NaCl concentration from 0.5 to 1 M, IBP degradation increased by 18% (see Figs. 5c) to 96.7% within 2.5 h [78].

The demonstration of near complete removal of IBP shows that the degradation of recalcitrant pollutants in WW using PEC based methods are often a function of treatment time. Other contributing factors include, active surface area, mass transfer and electrolyte type. Therefore, future research should focus on intensifying PEC WW treatment to improve their technology readiness and understanding its environmental impact, rather than focussing on new materials for incremental improvement in removal efficiencies.
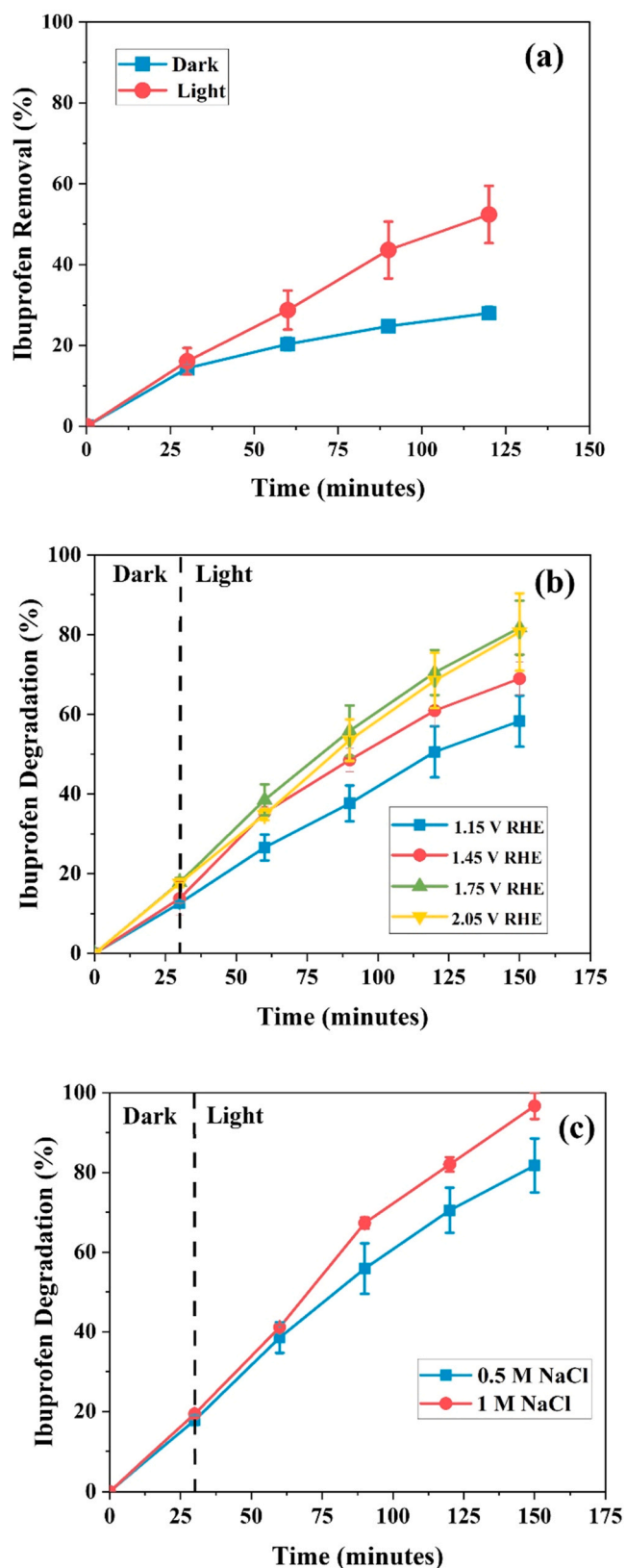
Fig. 5. (a) PEC ibuprofen degradation under the dark and light (1 Sun) at applied potential of 1.15 V vs RHE (0.5 M NaCl electrolyte). (b) PEC ibuprofen degradation carried out at different applied potentials. (c) Influence of NaCl concentration on PEC ibuprofen degradation performance measured at 1.15 V vs RHE. The correction bar is included in the respective results.

3.4. Elucidation of WO$_3$/BiVO$_4$ photoanode degradation mechanisms: IBP

Studies exploring PEC, PC and other advance oxidation processes have identified that different and often undesirable by-products can be generated from IBP degradation that are hazardous to aquatic life and potentially, human health. Hazardous substances include malonate, phenol, 4-isobutylacetophenone and hydroxy-ibuprofen (Table S2), and further underlines the importance of deciphering the degradative pathways using this new photoanode design to avoid their generation (if possible). The application of the developed WO$_3$/BiVO$_4$ photoanode generated several low mass species that spanned the hydrophobicity range of the positive ion chromatogram (see Fig. 6). This was expected, as it was evident within the single published paper [71] which explored PEC that identified ibuprofen was degraded to 2-Hydoxyl-propanoic acid, Hydroxyl-acetic acid, Pentanoic acid, Malonate, Phenol and 1, 4-Benzenedicarboxylic acid. However, rather than generating a protonated molecule ion species via electrospray ionisation-mass spectrometry (ESI-MS), this work involved the analysis of the IBP by-products using gas chromatography-mass spectrometry (GC-MS) (see Figs. S6 and S7), and as such, the fragmentation data obtained within this published work is not directly comparable to those observed via CID when using ESI-MS (Fig. S8). Therefore, the chromatogram of the acquired data obtained with this WO$_3$/BiVO$_4$ photoanode was first searched for equivalent precursor mass species for the known PEC by-products, and then cross refenced versus analogous photocatalyst technology measured via LC-MS for possible candidate identities (Table S2) [79].

Interestingly, the sample did not appear to show evidence of known PEC by-products but did indicate the presence of molecule ion species of *m/z* 239, 223, 221 and 177. When compared to the literature of other AO processes (including PC UV/advanced oxidation process), *m/z* 239, 223, and 177 matched formula of C$_{13}$H$_{18}$O$_4$, C$_{13}$H$_{18}$O$_3$, and C$_{12}$H$_{16}$O, respectively [80]. However, upon fragmentation the product ion spectra showed differences to those of the anticipated PC by-products, including toxic substances such as hydroxy-ibuprofen and 4-isobutylacetophenone (see table S2) identified in previous work [79]. Therefore, the data obtained from this new PEC photoanode indicates the potential formation of novel isobaric species to both published PC and PEC systems. To characterise these species, the fragmentation patterns were explored for losses commonly associated with the fragmentation of IBP by-products (see Table 1). This data suggested fragment ions were largely alkyl or oxygenated alkyl species, with only *m/z* 221, 177 showing evidence of aromaticity within the structure, indicated by the presence of a benzyl (*m/z* 77) and phenoxy fragment ion (*m/z* 93). Thus, this evidence indicates a substantial change in the chemical structure of IBP when treated with this PEC process with no confirmation of the known hazardous by-products being produced during the process.

Various species can be responsible for the degradation of IBP in a PEC system. To help determine the degradative mechanisms, identification of the type of oxidant is crucial. In general, photoholes at valence band of irradiated semiconductor catalyst surface are responsible for pollutant degradation directly or indirectly via free radicals or oxidant species [57, 71–72, 78, 81–82]. Thermodynamically, the main reactive species produced by the semiconductor catalyst would be •OH where the valence band maximum position of the semiconductor catalyst should be equal or above 2.32 V RHE [60]. The hydroxyl radical generation will only be prevalent when efficient charge separation occurs. Otherwise, with the higher rates of charge carrier recombination, the radical generation will be limited and oxidation can directly proceed via photoholes. This would especially be true when a higher adsorption of IBP is observed on the catalyst. In such a scenario, when the catalyst surface is saturated with the pollutant, surface adsorbed water molecules will be minimal thereby leading to negligible hydroxyl radical formation.

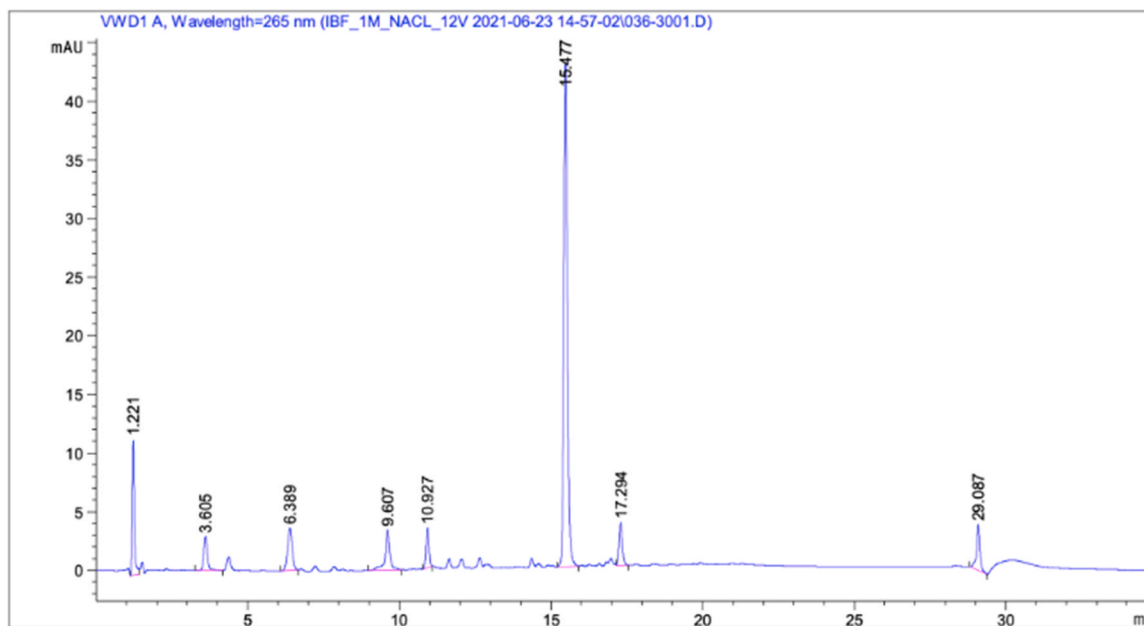Therefore, to identify the active reactive species on mesoporous

Fig. 6. The representative chromatogram was obtained from the final sample of the optimised PEC ibuprofen degradation experiment.

Table 1

Summarises the m/z of the precursor ion species with their corresponding product ions obtained by CID fragmentation. Unk – unknown.

Precursor Ion (m/z)	Major Product Ion Identified (m/z)	Tentative Product Ion Assignment	Mass Loss
239	198	$C_{13}H_{26}O$	41
	157	$C_{10}H_{21}O$	82
	116	$C_7H_{16}O$	123
	95	$C_4H_{15}O_2$	144
	93	$C_4H_{13}O_2$	146
	77	$C_4H_{13}O$	162
	75	$C_4H_{11}O$	164
	73	C_4H_9O	166
223	149	Unk	74
	57	C_4H_9	166
221	139	Unk	82
	133	Unk	88
	105	C_7H_5O	116
	57	C_4H_9	164
177	149	$C_{11}H_{16}$	28
	134	$C_{10}H_{13}$	43
	77	C_6H_5	100
	57	C_4H_9	120

WO$_3$/BiVO$_4$ photoanode, a coumarin probe-based method was utilised. When hydroxyl radicals are the predominant reactive species, coumarin will be hydroxylated to generated hydroxycoumarins [83,84]. This experiment utilised 100 μM of coumarin to capture any OH• radicals that may be generated in the system. The product of interest, umbelliferone (also known as 7-hydroxycoumarin) was fluorometrically quantified (emission peak 450 nm, excitation peak 332 nm) to determine the hydroxyl radical producing ability of the system [83,85].

The PEC coumarin degradation concerning the duration of the reactions is presented in Fig. 7a. It seems WO$_3$/BiVO$_4$ effectively degraded 50% of coumarin in 60 min of light irradiation. The PL spectra (Fig. 7b) resulted in weak peaks at 450 nm. Alongside, the area under the curve was observed to increase with time indicating that there may negligible formation of umbelliferone which is consistent with literature for WO$_3$ based catalysts [86]. This argument also aligns with other research reports where the inadequate valence band position of BiVO$_4$ does not support •OH radical generation until adding the scavengers in the electrolyte or surface modification [87–89]. The heterostructure

formation on BiVO$_4$ surface with WO$_3$ may have induced weak hydroxyl radical production ability of the photoanode. Furthermore, the rate of coumarin degradation seems to be declining beyond 60 min (Fig. 8a) suggesting that there may have been competitive adsorption on the anode surface by the intermediates formed. These intermediates could be other non-fluorescent hydroxycoumarins or other coumarin degradation products [86]. This suggests that in addition to hydroxyl radicals, other reactive oxidants may have also contributed to the degradation of IBP in this system.

Another probable oxidant that may be prevalent in BiVO$_4$ based PEC systems is hydrogen peroxide. Recent reports show that BiVO$_4$ is capable of producing anodic hydrogen peroxide via the traditional PEC water splitting process as follows [90–94],

$$2\,H_2O \rightarrow H_2O_2 + 2\,H^+ + 2e^- \quad E_0(H_2O_2/H_2O) = +1{\cdot}78 \text{ V vs·RHE} \quad (1)$$
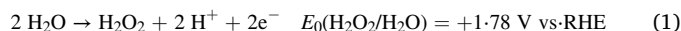
Further, we investigated the electrolyte and ensured the hydrogen peroxide formation using Quantofix hydrogen peroxide strips to determine the approximate concentration of hydrogen peroxide in mg/L. A colour change in the strips indicated the hydrogen peroxide formation (Fig. S9). The results are presented in Fig. 8. A significant amount of hydrogen peroxide formation in the electrolyte was confirmed during PEC reactions, which increased between 1.5 and 2.3 mg/L with the reaction duration.

In general, the water oxidation to oxygen evolution competes with hydrogen peroxide formation at the BiVO$_4$ photoanode with the selectivity depending on the semiconductor material [95]. In BiVO$_4$, hydrogen peroxide formation can be achieved by surface passivation layer coating, which modulates the surface hole oxidation reaction kinetics to suppress the oxygen evolution. But in our case, organic pollutants at the photoanode compartment act as an electron donor to the BiVO$_4$, effectively scavenging the photo holes and thus preventing water oxidation. Fuku et al [94]. suggested that in-situ PEC hydrogen peroxide generation at electrodes can oxidise organic species such as IBP. Therefore Fig. 8 unambiguously explains anodic hydrogen peroxide formation at BiVO$_4$ which could be the predominant oxidant responsible for IBP degradation. To the best of our knowledge, this is the first-time, involvement of hydrogen peroxide was experimentally observed in WO$_3$/BiVO$_4$-based PEC IBP degradation experiments. This PEC in-situ hydrogen peroxide generation-based IBP pollutants degradation will be economically advantageous compared with hybrid process of UV
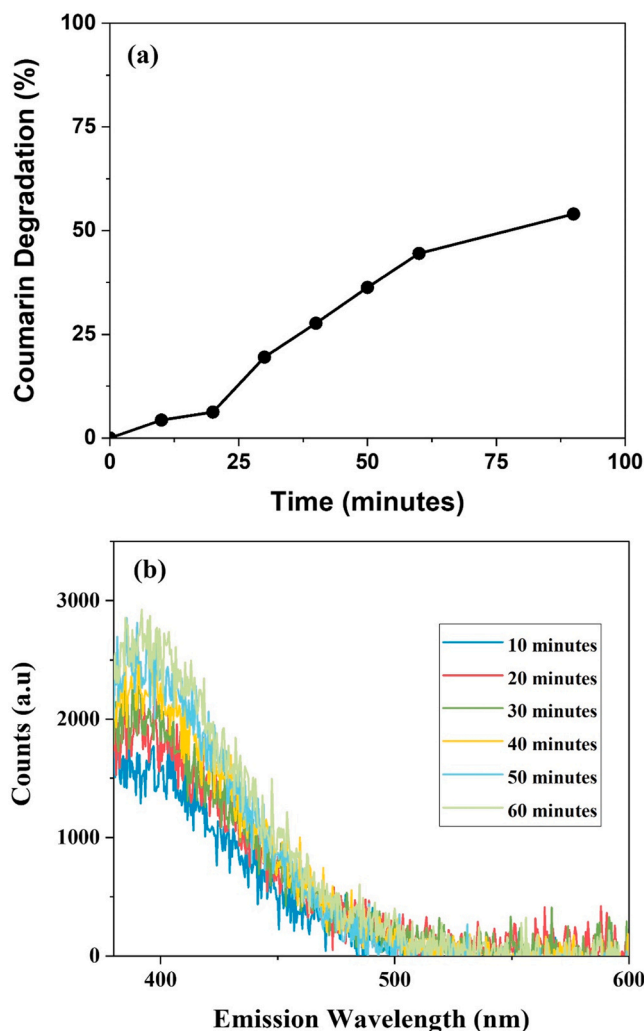
Fig. 7. (a) A graph displaying the PEC coumarin degradation achieved by the WO$_3$/BiVO$_4$ photoanode, and (b) The PL spectra obtained during the coumarin degradation experiment.
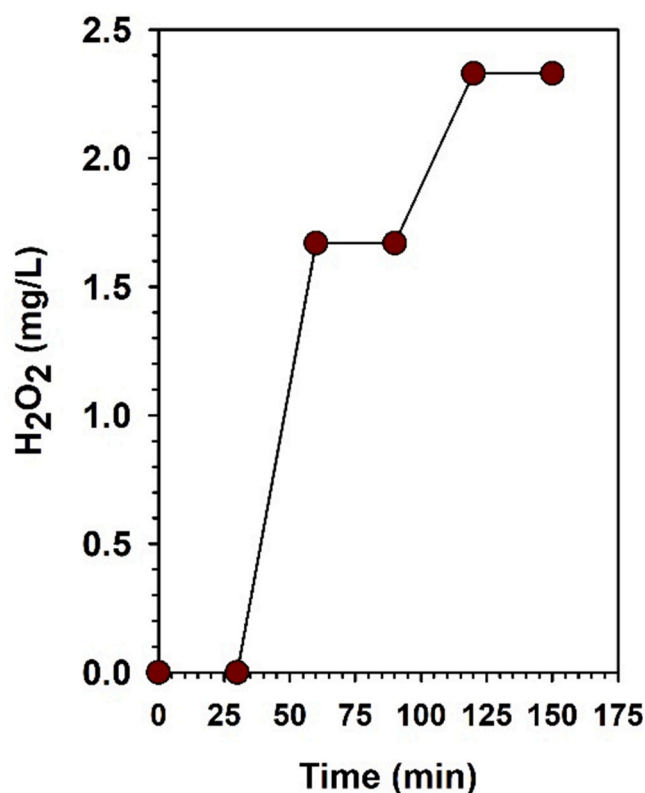

Fig. 8. Approximate quantification of the hydrogen peroxide concentration in the electrolyte solution during the ibuprofen degradation process. The experimental values obtained for average of three runs.

ozone + hydrogen peroxide based IBP degradation where commercial hydrogen peroxide was added externally [96].

The stability of the mesoporous WO$_3$/BiVO$_4$ photoanodes was tested in at least three IBP degradation runs (Fig. S7). The degradation performance was reduced with every subsequent run. It might have been due to the photo hole accumulation at the photoanode resulting in photooxidation of BiVO$_4$ and the dissolution of V^{5+} to the electrolyte, which drives photocorrosion at the photoanode [97]. The deposition of porous and ion-permeable catalysts such as Co-Pi, FeOOH, NiOOH or FeNiOOH, etc., on BiVO$_4$ can improve the extraction of photogenerated holes from the near-surface region, which can effectively reduce photocorrosion of the semiconductor catalyst surface [98–100]. Another reason is that the electrolyte's pH changes (Fig. S10) during the PEC process, which may also affect the stability of BiVO$_4$. The estimated Pourbaix diagram by Toma et al [98]. shows that BiVO$_4$ can be stable for a wide range of potentials and pH 4 <pH< 11. But in this work, the pH of the electrolyte after PEC treatment was reduced to lower than 4, which might have affected the stability of the photoanode. In previous reports of photocatalytic IBP degradation, this issue is not adequately discussed. This issue also can be overcome with co-catalyst coating on photoanode [101]. Therefore stability of BiVO$_4$ photoanode can be further improved with metal oxide-based passivation layer coatings on top of the BiVO$_4$ surface [95], or metal doping at BiVO$_4$ [102]. The pH of the electrolyte reduced from 4.3 to 2.1 after the PEC IBP degradation,

indicating that it should be neutralised before being discharged from the treatment plants.

To further improve the economics of PEC wastewater treatment, co-generation of hydrogen gas at the cathode compartment during the PEC IBP degradation process was demonstrated and the generated H$_2$ was quantified by gas chromatography. Initially, PEC water splitting (without pollutants) at the WO$_3$/BiVO$_4$ photoanode was investigated. Fig. S9 shows that hydrogen gas was observed at the cathode compartment under illumination, but no hydrogen gas was noticed in dark conditions. It validates the PEC water-splitting activity at WO$_3$/BiVO$_4$-based PEC cells. Further, Fig. 9 demonstrates that the PEC systems could generate a similar amount of hydrogen gas in the presence and absence of IBP in the electrolyte (anode compartment). For instance, the PEC IBP degradation process produced ~61 $\pm$ 5.5 μmol/cm^2 of hydrogen whilst simultaneously degrading ibuprofen in the water, similar to ~69 $\pm$ 5.5 μmol/cm^2 in the absence of IBP in the electrolyte (within the error limits), implying IBP has little effect on the H$_2$ generation. However, increasing the IBP concentration further may be expected to increase the proton concentration in the anode compartment, thus enhancing the hydrogen generation at the cathode. The usage of the Nafion membrane in the PEC cells successfully separates the ibuprofen degradation reactions (at the anode) from the hydrogen production (at the cathode). If the membrane were absent, the secondary by-products from ibuprofen degradation would further reduce as the cathode surface, which would be a competitive reaction for hydrogen gas production.

As can be seen, the enhanced PEC IBP degradation rate after increasing NaCl concentration (Fig. 5c) was expected to produce more protons (H$^+$) as by-products in the photoanode compartment. The increased proton concentration from the PEC IBP degradation reactions could enhance the hydrogen gas evolution at the cathode. As expected, the hydrogen gas evolution was markedly increased from ~61 μmol/cm^2 to ~114 $\pm$ 5.5 μmol/cm^2 for 145 min of the PEC reactions period at
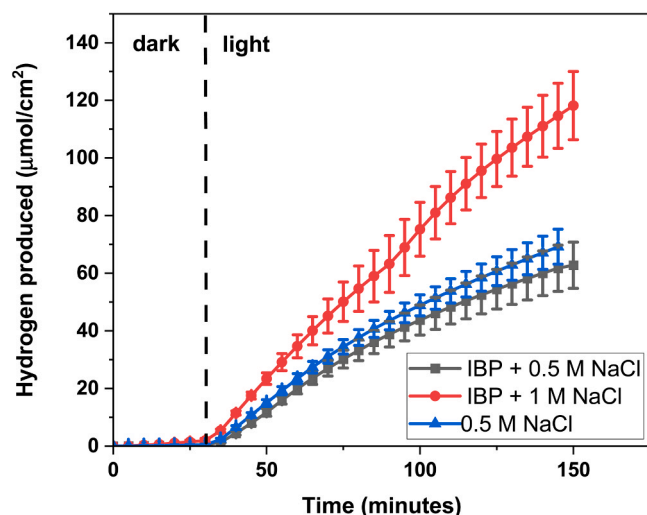
Fig. 9. PEC hydrogen production in the presence and absence of ibuprofen (IBP) in the electrolyte. Note that the PEC cells encompass WO₃/BiVO₄ photoanode, Pt mesh counter electrode, and Ag/AgCl reference electrode. The PEC hydrogen generation measurements were carried out at 1 sun irradiation under 1.75 V vs. RHE applied potential.

1.75 V vs. RHE applied potential. The 2-fold enhanced hydrogen gas evolution by increasing the NaCl concentration from 0.5 to 1 M in the electrolyte demonstrates the importance of electrolyte conductivity at BiVO₄ via electrolyte engineering.

IBP degradation has been investigated predominantly via hybrid advanced oxidation processes due to its recalcitrance. Most of the reported literature use H_2O_2 as an external oxidant to enhance the IBP degradation efficiencies [103–105]. [57,96], For instance, photocatalysis based methods utilise one reaction chamber and therefore are prone to higher charge carrier recombination as well as toxic intermediate product formation. From a safety and operations cost point of view, it is not advisable to utilise externally added peroxide for pollutant degradation. Therefore, recent research has focussed on in situ generation and utilisation of H_2O_2 for IBP removal from wastewater (refer to Table S4) [106–108]. Along these lines, we have demonstrated complete IBP removal via the PEC based process involving in situ H_2O_2 generation. In addition to complete IBP degradation, the intermediate product analysis show that no hazardous products were formed as a result as compared to previously reported works [103,105]. While there are no previous studies to directly compare PEC based IBP degradation with in situ H_2O_2 generation, a general comparison of existing literature with hybrid advanced oxidation processes presented in Table S4 showed that the results presented in this work are on par with current state of the art. Furthermore, the use of mesoporous WO₃/BiVO₄ photoanode for IBP degradation alongside simultaneous H_2 production at the cathode was also reported for the first time.

The schematic illustration of simultaneous IBP degradation at the anode compartment and hydrogen gas generation at the cathode compartment is previously explained in Scheme 1. Briefly, photoholes forms oxidants (hydrogen peroxide) and H^+ as a by-product in the anodic compartment. The hydrogen peroxide produced in-situ, oxidises IBP to generate intermediates. The H^+ ions are transferred to the cathodic compartment via the proton exchange membrane, where the photoelectrons transported to the Pt cathode reduce H^+ to generate hydrogen gas.

Overall, the experimental results presented in Figs. 5c and 9 confirmed the feasibility of simultaneous green hydrogen evolution from the PEC IBP degradation process (anode). The photocorrosive behaviour observed at the BiVO₄ surface can be further suppressed with a passivation layer coating or co-catalyst decoration. Enhancing the charge separation, i.e., photoholes from BiVO₄ to the electrolyte via

surface engineering is anticipated to avoid further corrosion.

4. Conclusions

The application of a mesoporous nanoscale WO₃/BiVO₄ photoanode was demonstrated in PEC water splitting and IBP degradation. The WO₃/BiVO₄ photoanode showed up to 96.7% of IBP degradation within 150 min when a NaCl-based electrolyte was used. However, the chemical analysis of the electrolyte after PEC treatment warned that 4-Isobutylacetophenone was formed as a primary intermediate. It could however be possible to completely eliminate this intermediate by extending the PEC process duration above 150 min. It was also further demonstrated that unlike reported in the literature, IBP degradation did not proceed via a OH• radical based mechanism, but rather progressed via a H_2O_2 based oxidation pathway. Furthermore, concurrent generation of green hydrogen ($\sim$114 µmol/cm^2) was also demonstrated alongside IBP degradation at 145 min of reaction period under 1.75 V vs. RHE applied potential. The demonstration of tandem reaction suggests that PEC is a viable technology for recovering energy from wastewater. This work opens a platform for designing efficient photoelectrocatalyst materials for tackling toxic organic water pollutants, including pharmaceutical species and recovering green hydrogen gas to support the net zero transition.

Declaration of Competing Interest

There are no conflicts to declare.

Data availability

The data that has been used is confidential.

Appendix A. Supporting information

Supplementary data associated with this article can be found in the online version at doi:10.1016/j.jece.2023.110256.

References

[1] OECD, Pharmaceutical Residues in Freshwater, 2019.

[2] D. O'Flynn, J. Lawler, A. Yusuf, A. Parle-McDermott, D. Harold, T. Mc Cloughlin, L. Holland, F. Regan, B. White, A review of pharmaceutical occurrence and pathways in the aquatic environment in the context of a changing climate and the COVID-19 pandemic, Anal. Methods 13 (2021) 575–594.

[3] J.L. Wilkinson, A.B.A. Boxall, D.W. Kolpin, K.M.Y. Leung, R.W.S. Lai, C. Galbán-Malagón, A.D. Adell, J. Mondon, M. Metian, R.A. Marchant, A. Bouzas-Monroy, A. Cuni-Sanchez, A. Coors, P. Carriquiriborde, M. Rojo, C. Gordon, M. Cara, M. Moermond, T. Luarte, V. Petrosyan, Y. Perikhanyan, C.S. Mahon, C.J. McGurk, T. Hofmann, T. Kormoker, V. Iniguez, J. Guzman-Otazo, J.L. Tavares, F. Gildasio De Figueiredo, M.T.P. Razzolini, V. Dougnon, G. Gbaguidi, O. Traoré, J.M. Blais, L.E. Kimpe, M. Wong, D. Wong, R. Ntchantcho, J. Pizarro, G.-G. Ying, C.-E. Chen, M. Páez, J. Martínez-Lara, J.-P. Otamonga, J. Poté, S.A. Ifo, P. Wilson, S. Echeverría-Sáenz, N. Udikovic-Kolic, M. Milakovic, D. Fatta-Kassinos, L. Ioannou-Ttofa, V. Belušová, J. Vymazal, M. Cárdenas-Bustamante, B.A. Kassa, J. Garric, A. Chaumot, P. Gibba, I. Kunchulia, S. Seidensticker, G. Lyberatos, H.P. Halldórsson, M. Melling, T. Shashidhar, M. Lamba, A. Nastiti, A. Supriatin, N. Pourang, A. Abedini, O. Abdullah, S.S. Gharbia, F. Pilla, B. Chefetz, T. Topaz, K.M. Yao, B. Aubakirova, R. Beisenova, L. Olaka, J.K. Mulu, P. Chatanga, V. Ntuli, N.T. Blama, S. Sherif, A.Z. Aris, L.J. Looi, M. Niang, S.T. Traore, R. Oldenkamp, O. Ogunbanwo, M. Ashfaq, M. Iqbal, Z. Abdeen, A. O'Dea, J.M. Morales-Saldaña, M. Custodio, H. de la Cruz, I. Navarrete, F. Carvalho, A.B. Gogra, B.M. Koroma, V. Cerkvenik-Flajs, M. Gombač, M. Thwala, K. Choi, H. Kang, J.L.C. Ladu, A. Rico, P. Amerasinghe, A. Sobek, G. Horlitz, A.K. Zenker, A.C. King, J.-J. Jiang, R. Kariuki, M. Tumbo, U. Tezel, T.T. Onay, J.B. Lejju, Y. Vystavna, Y. Vergeles, H. Heinzen, A. Pérez-Parada, D.B. Sims, M. Figy, D. Good, C. Teta, Pharmaceutical pollution of the world's rivers, Proceedings of the National Academy of Sciences 119, 2022: e2113947119.

[4] B. Quinn, F. Gagné, C. Blaise, An investigation into the acute and chronic toxicity of eleven pharmaceuticals (and their solvents) found in wastewater effluent on the cnidarian, Hydra attenuata, Sci. Total Environ. 389 (2008) 306–314.

[5] K.M. Gaworecki, S.J. Klaine, Behavioral and biochemical responses of hybrid striped bass during and after fluoxetine exposure, Aquat. Toxicol. 88 (2008) 207–213.

[6] G. Nentwig, Effects of Pharmaceuticals on Aquatic Invertebrates. Part II: The Antidepressant Drug Fluoxetine, Arch. Environ. Contam. Toxicol. 52 (2007) 163–170.

[7] C.B. Patneedi, K. Prasadu, Impact Pharm. Wastes Hum. Life Environ. 8 (2015) 67–70.

[8] M. Patel, R. Kumar, K. Kishor, T. Mlsna, C.U. Pittman Jr., D. Mohan, Pharmaceuticals of Emerging Concern in Aquatic Systems: Chemistry, Occurrence, Effects, and Removal Methods, Chem. Rev. 119 (2019) 3510–3673.

[9] M. Miettinen, S.A. Khan, Pharmaceutical pollution: A weakly regulated global environmental risk, Review of European, Comp. Int. Environ. Law 31 (2022) 75–88.

[10] A.J. Ebele, M. Abou-Elwafa Abdallah, S. Harrad, Pharmaceuticals and personal care products (PPCPs) in the freshwater aquatic environment, Emerg. Contam. 3 (2017) 1–16.

[11] A. Marchlewicz, U. Guzik, D. Wojcieszyńska, Over-the-Counter Monocyclic Non-Steroidal Anti-Inflammatory Drugs in Environment-Sources, Risks, Biodegradation, Water Air Soil Pollut. 226 (2015), 355–355.

[12] P. Guerra, M. Kim, A. Shah, M. Alaee, S.A. Smyth, Occurrence and fate of antibiotic, analgesic/anti-inflammatory, and antifungal compounds in five wastewater treatment processes, Sci. Total Environ. 473–474 (2014) 235–243.

[13] Ld.M. Pirete, F.P. Camargo, G.M. Grosseli, I.K. Sakamoto, P.S. Fadini, E.L. Silva, M.B.A. Varesche, Influence of ethanol and nitrate on ibuprofen removal in batch reactors under denitrifying conditions, Process Saf. Environ. Prot. 160 (2022) 297–309.

[14] S. Chopra, D. Kumar, Ibuprofen as an emerging organic contaminant in environment, distribution and remediation, Heliyon 6 (2020), e04087.

[15] M. Gonzalez-Rey, M.J. Bebianno, Does non-steroidal anti-inflammatory (NSAID) ibuprofen induce antioxidant stress and endocrine disruption in mussel Mytilus galloprovincialis? Environ. Toxicol. Pharmacol. 33 (2012) 361–371.

[16] H.J. De Lange, W. Noordoven, A.J. Murk, M. Lürling, E.T.H.M. Peeters, Behavioural responses of Gammarus pulex (Crustacea, Amphipoda) to low concentrations of pharmaceuticals, Aquat. Toxicol. 78 (2006) 209–216.

[17] J. Du, C.-F. Mei, G.-G. Ying, M.-Y. Xu, Toxicity Thresholds for Diclofenac, Acetaminophen and Ibuprofen in the Water Flea Daphnia magna, Bull. Environ. Contam. Toxicol. 97 (2016) 84–90.

[18] G. Divyapriya, S. Singh, C.A. Martínez-Huitle, J. Scaria, A.V. Karim, P. V. Nidheesh, Treatment of real wastewater by photoelectrochemical methods: An overview, Chemosphere 276 (2021), 130188.

[19] B.A. Koiki, B.O. Orimolade, B.N. Zwane, D. Nkosi, N. Mabuba, O.A. Arotiba, Cu₂O on anodised TiO₂ nanotube arrays: A heterojunction photoanode for visible light assisted electrochemical degradation of pharmaceuticals in water, Electrochim. Acta 340 (2020), 135944.

[20] J. Liu, J. Li, Y. Li, J. Guo, S.-M. Xu, R. Zhang, M. Shao, Photoelectrochemical water splitting coupled with degradation of organic pollutants enhanced by surface and interface engineering of BiVO₄ photoanode, Appl. Catal. B: Environ. 278 (2020), 119268.

[21] P.J. Mafa, A.T. Kuvarega, B.B. Mamba, B. Ntsendwana, Photoelectrocatalytic degradation of sulfamethoxazole on g-C₃N₄/BiOI/EG p-n heterojunction photoanode under visible light irradiation, Appl. Surf. Sci. 483 (2019) 506–520.

[22] N. Haddadou, N. Bensemma, G. Rekhila, M. Trari, K. Taïbi, Photoelectrochemical investigations in lead-free Ba (Ti₀.₉₅₀Sc₀.₀₂₅Nb₀.₀₂₅)O₃ ferroelectric ceramics. Application to amoxicillin photodegradation, J. Photochem. Photobiol. A: Chem. 358 (2018) 294–299.

[23] A.J. Bard, Photoelectrochemistry, Science 207 (1980) 139–144.

[24] M. Grätzel, Photoelectrochemical cells, Nature 414 (2001) 338–344.

[25] S. Pitchaimuthu, K. Sridharan, S. Nagarajan, S. Ananthraj, P. Robertson, M. F. Kuehnel, Á. Irabien, M. Maroto-Valer, Solar Hydrogen Fuel Generation from Wastewater—Beyond Photoelectrochemical Water Splitting: A Perspective, Energies 15 (2022) 7399.

[26] T.H. Jeon, M.S. Koo, H. Kim, W. Choi, Dual-Functional Photocatalytic and Photoelectrocatalytic Systems for Energy- and Resource-Recovering Water Treatment, ACS Catal. 8 (2018) 11542–11563.

[27] S. Kampouri, K.C. Stylianou, Dual-Functional Photocatalysis for Simultaneous Hydrogen Production and Oxidation of Organic Substances, ACS Catal. 9 (2019) 4247–4270.

[28] S. Nagarajan, R.J. Jones, L. Oram, J. Massanet-Nicolau, A. Guwy, Intensification of Acidogenic Fermentation for the Production of Biohydrogen and Volatile Fatty Acids—A Perspective, Fermentation 8 (2022) 325.

[29] K. de Kleijne, H. de Coninck, R. van Zelm, M.A.J. Huijbregts, S.V. Hanssen, The many greenhouse gas footprints of green hydrogen, Sustain. Energy Fuels 6 (2022) 4383–4387.

[30] K. Bareiß, C. de la Rua, M. Möckl, T. Hamacher, Life cycle assessment of hydrogen from proton exchange membrane water electrolysis in future energy systems, Appl. Energy 237 (2019) 862–872.

[31] R.R. Beswick, A.M. Oliveira, Y. Yan, Does the Green Hydrogen Economy Have a Water Problem? ACS Energy Lett. 6 (2021) 3167–3169.

[32] T. Li, T. Kasahara, J. He, K.E. Dettelbach, G.M. Sammis, C.P. Berlinguette, Photoelectrochemical oxidation of organic substrates in organic media, Nat. Commun. 8 (2017) 390.

[33] I. Grigioni, G. Di Liberto, M.V. Dozzi, S. Tosoni, G. Pacchioni, E. Selli, WO₃/BiVO₄ Photoanodes: Facets Matching at the Heterojunction and BiVO₄ Layer Thickness Effects, ACS Appl. Energy Mater. 4 (2021) 8421–8431.

[34] M. Hepel, J. Luo, Photoelectrochemical mineralization of textile diazo dye pollutants using nanocrystalline WO₃ electrodes, Electrochim. Acta 47 (2001) 729–740.

[35] G. Waldner, A. Brüger, N.S. Gaikwad, M. Neumann-Spallart, WO₃ thin films for photoelectrochemical purification of water, Chemosphere 67 (2007) 779–784.

[36] K. Dai, L. Lu, C. Liang, Q. Liu, G. Zhu, Heterojunction of facet coupled g-C₃N₄/surface-fluorinated TiO₂ nanosheets for organic pollutants degradation under visible LED light irradiation, Appl. Catal. B: Environ. 156 157 (2014) 331–340.

[37] B. Baral, K.H. Reddy, K.M. Parida, Construction of M-BiVO₄/T-BiVO₄ isotype heterojunction for enhanced photocatalytic degradation of Norfloxacine and Oxygen evolution reaction, J. Colloid Interface Sci. 554 (2019) 278–295.

[38] Y. Hou, G. Yuan, S. Wang, Z. Yu, S. Qin, L. Tu, Y. Yan, X. Chen, H. Zhu, Y. Tang, Nitrofurazone degradation in the self-biased bio-photoelectrochemical system: g-C₃N₄/CdS photocathode characterization, degradation performance, mechanism and pathways, J. Hazard. Mater. 384 (2020), 121438.

[39] M. Wang, Y. Yang, J. Shen, J. Jiang, L. Sun, Visible-light-absorbing semiconductor/molecular catalyst hybrid photoelectrodes for H₂ or O₂ evolution: recent advances and challenges, Sustain. Energy Fuels 1 (2017) 1641–1663.

[40] M.-J. Choi, T.L. Kim, K.S. Choi, W. Sohn, T.H. Lee, S.A. Lee, H. Park, S.Y. Jeong, J. W. Yang, S. Lee, H.W. Jang, Controlled Band Offsets in Ultrathin Hematite for Enhancing the Photoelectrochemical Water Splitting Performance of Heterostructured Photoanodes, ACS Appl. Mater. Interfaces 14 (2022) 7788–7795.

[41] S. Li, W. Xu, L. Meng, W. Tian, L. Li, Recent Progress on Semiconductor Heterojunction-Based Photoanodes for Photoelectrochemical Water Splitting, Small Sci. 2 (2022) 2100112.

[42] J. Choi, P. Sudhagar, J.H. Kim, J. Kwon, J. Kim, C. Terashima, A. Fujishima, T. Song, U. Paik, WO₃/W:BiVO₄/BiVO₄ graded photoabsorber electrode for enhanced photoelectrocatalytic solar light driven water oxidation, Phys. Chem. Chem. Phys. 19 (2017) 4648–4655.

[43] P.M. Rao, L. Cai, C. Liu, I.S. Cho, C.H. Lee, J.M. Weisse, P. Yang, X. Zheng, Simultaneously Efficient Light Absorption and Charge Separation in WO₃/BiVO₄ Core/Shell Nanowire Photoanode for Photoelectrochemical Water Oxidation, Nano Lett. 14 (2014) 1099–1105.

[44] Q. Zeng, J. Li, L. Li, J. Bai, L. Xia, B. Zhou, Synthesis of WO₃/BiVO₄ photoanode using a reaction of bismuth nitrate with peroxovanadate on WO₃ film for efficient photoelectrocatalytic water splitting and organic pollutant degradation, Appl. Catal. B: Environ. 217 (2017) 21–29.

[45] B.S. Kalanoor, H. Seo, S.S. Kalanur, Recent developments in photoelectrochemical water-splitting using WO₃/BiVO₄ heterojunction photoanode: A review, Mater. Sci. Energy Technol. 1 (2018) 49–62.

[46] X. Shi, I.Y. Choi, K. Zhang, J. Kwon, D.Y. Kim, J.K. Lee, S.H. Oh, J.K. Kim, J. H. Park, Efficient photoelectrochemical hydrogen production from bismuth vanadate-decorated tungsten trioxide helix nanostructures, Nat. Commun. 5 (2014) 4775.

[47] V. Cristino, L. Pasti, N. Marchetti, S. Berardi, C.A. Bignozzi, A. Molinari, F. Passabi, S. Caramori, L. Amidani, M. Orlandi, N. Bazzanella, A. Piccioni, J. Kopula Kesavan, F. Boscherini, L. Pasquini, Photoelectrocatalytic degradation of emerging contaminants at WO₃/BiVO₄ photoanodes in aqueous solution, Photochem. Photobiol. Sci. 18 (2019) 2150–2163.

[48] L. Zhou, C. Zhao, B. Giri, P. Allen, X. Xu, H. Joshi, Y. Fan, L.V. Titova, P.M. Rao, High Light Absorption and Charge Separation Efficiency at Low Applied Voltage

from Sb-Doped SnO₂/BiVO₄ Core/Shell Nanorod-Array Photoanodes, Nano Lett. 16 (2016) 3463–3474.

[49] H.W. Jeong, T.H. Jeon, J.S. Jang, W. Choi, H. Park, Strategic Modification of BiVO₄ for Improving Photoelectrochemical Water Oxidation Performance, J. Phys. Chem. C. 117 (2013) 9104–9112.

[50] L. Cai, J. Zhao, H. Li, J. Park, I.S. Cho, H.S. Han, X. Zheng, One-Step Hydrothermal Deposition of Ni:FeOOH onto Photoanodes for Enhanced Water Oxidation, ACS Energy Lett. 1 (2016) 624–632.

[51] S.J. Hong, S. Lee, J.S. Jang, J.S. Lee, Heterojunction BiVO₄/WO₃ electrodes for enhanced photoactivity of water oxidation, Energy Environ. Sci. 4 (2011) 1781–1787.

[52] J. Su, L. Guo, N. Bao, C.A. Grimes, Nanostructured WO₃/BiVO₄ Heterojunction Films for Efficient Photoelectrochemical Water Splitting, Nano Lett. 11 (2011) 1928–1933.

[53] S.Y. Chae, C.S. Lee, H. Jung, O.-S. Joo, B.K. Min, J.H. Kim, Y.J. Hwang, Insight into Charge Separation in WO₃/BiVO₄ Heterojunction for Solar Water Splitting, ACS Appl. Mater. Interfaces 9 (2017) 19780–19790.

[54] Q. Pan, H. Zhang, Y. Yang, C. Cheng, 3D Brochosomes-Like TiO₂/WO₃/BiVO₄ Arrays as Photoanode for Photoelectrochemical Hydrogen Production, Small 15 (2019) 1900924.

[55] X. Yao, X. Hu, Y. Liu, X. Wang, X. Hong, X. Chen, S.C. Pillai, D.D. Dionysiou, D. Wang, Simultaneous photocatalytic degradation of ibuprofen and H₂ evolution over Au/sheaf-like TiO2 mesocrystals, Chemosphere 261 (2020), 127759.

[56] C.-H. Chen, Y.-C. Lin, Y.-P. Peng, M.-H. Lin, Simultaneous hydrogen production and ibuprofen degradation by green synthesized Cu₂O/TNTAs photoanode, Chemosphere 284 (2021), 131360.

[57] Q. Sun, Y.-P. Peng, H. Chen, K.-L. Chang, Y.-N. Qiu, S.-W. Lai, Photoelectrochemical oxidation of ibuprofen via Cu₂O-doped TiO₂ nanotube arrays, J. Hazard. Mater. 319 (2016) 121–129.

[58] A. Sahmi, K. Bensadok, B. Zirour, M. Trari, Physical and photoelectrochemical characterizations of SrWO₄ prepared by thermal decomposition. Application to the photo electro-oxidation of ibuprofen, J. Solid State Electrochem. 21 (2017) 2817–2824.

[59] Y.-P. Peng, C.-C. Liu, K.-F. Chen, C.-P. Huang, C.-H. Chen, Green synthesis of nano-silver–titanium nanotube array (Ag/TNA) composite for concurrent ibuprofen degradation and hydrogen generation, Chemosphere 264 (2021), 128407.

[60] K.R. Davies, Y. Cherif, G.P. Pazhani, S. Anantharaj, H. Azzi, C. Terashima, A. Fujishima, S. Pitchaimuthu, The upsurge of photocatalysts in antibiotic micropollutants treatment: Materials design, recovery, toxicity and bioanalysis, J. Photochem. Photobiol. C: Photochem. Rev. 48 (2021), 100437.

[61] B. O'Regan, M. Grätzel, A low-cost, high-efficiency solar cell based on dye-sensitized colloidal TiO₂ films, Nature 353 (1991) 737–740.

[62] S.S. Kalanur, L.T. Duy, H. Seo, Recent Progress in Photoelectrochemical Water Splitting Activity of WO₃ Photoanodes, Top. Catal. 61 (2018) 1043–1076.

[63] P. Wei, Y. Wen, K. Lin, X. Li, 2D/3D WO₃/BiVO₄ heterostructures for efficient photoelectrochemical water splitting, Int. J. Hydrog. Energy 46 (2021) 27506–27515.

[64] P. Chatchai, Y. Murakami, S.-y Kishioka, A.Y. Nosaka, Y. Nosaka, Efficient photocatalytic activity of water oxidation over WO₃/BiVO₄ composite under visible light irradiation, Electrochim. Acta 54 (2009) 1147–1152.

[65] Y. Liu, B.R. Wygant, K. Kawashima, O. Mabayoje, T.E. Hong, S.-G. Lee, J. Lin, J.-H. Kim, K. Yubuta, W. Li, J. Li, C.B. Mullins, Facet effect on the photoelectrochemical performance of a WO₃/BiVO₄ heterojunction photoanode, Appl. Catal. B: Environ. 245 (2019) 227–239.

[66] W. Nareejun, C. Ponchio, Novel photoelectrocatalytic/solar cell improvement for organic dye degradation based on simple dip coating WO₃/BiVO₄ photoanode electrode, Sol. Energy Mater. Sol. Cells 212 (2020), 110556.

[67] S. Darmawi, S. Burkhardt, T. Leichtweiss, D.A. Weber, S. Wenzel, J. Janek, M. T. Elm, P.J. Klar, Correlation of electrochromic properties and oxidation states in nanocrystalline tungsten trioxide, Phys. Chem. Chem. Phys. 17 (2015) 15903–15911.

[68] S. Xu, D. Fu, K. Song, L. Wang, Z. Yang, W. Yang, H. Hou, One-dimensional WO₃/BiVO₄ heterojunction photoanodes for efficient photoelectrochemical water splitting, Chem. Eng. J. 349 (2018) 368–375.

[69] S. Crawford, E. Thimsen, P. Biswas, Impact of Different Electrolytes on Photocatalytic Water Splitting, J. Electrochem. Soc. 156 (2009) H346.

[70] K.R. Tolod, S. Hernández, M. Castellino, F.A. Deorsola, E. Davarpanah, N. Russo, Optimization of BiVO₄ photoelectrodes made by electrodeposition for sun-driven water oxidation, Int. J. Hydrog. Energy 45 (2020) 605–618.

[71] H. Chen, Y.-P. Peng, T.-Y. Chen, K.-F. Chen, K.-L. Chang, Z. Dang, G.-N. Lu, H. He, Enhanced photoelectrochemical degradation of Ibuprofen and generation of hydrogen via BiOI-deposited TiO₂ nanotube arrays, Sci. Total Environ. 633 (2018) 1198–1205.

[72] K.-L. Chang, Q. Sun, Y.-P. Peng, S.-W. Lai, M. Sung, C.-Y. Huang, H.-W. Kuo, J. Sun, Y.-C. Lin, Cu₂O loaded titanate nanotube arrays for simultaneously photoelectrochemical ibuprofen oxidation and hydrogen generation, Chemosphere 150 (2016) 605–614.

[73] A. Hankin, F.E. Bedoya-Lora, J.C. Alexander, A. Regoutz, G.H. Kelsall, Flat band potential determination: avoiding the pitfalls, J. Mater. Chem. A 7 (2019) 26162–26176.

[74] L. Wang, Z. Liu, X. Xu, Y. Jia, Q. Mei, F. Ding, J. Peng, Q. Wang, Efficient Solar Water Splitting via Enhanced Charge Separation of the BiVO₄ Photoanode, ACS Appl. Energy Mater. 5 (2022) 6383–6392.

[75] D. Liu, J. Zhou, J. Wang, R. Tian, X. Li, E. Nie, X. Piao, Z. Sun, Enhanced visible light photoelectrocatalytic degradation of organic contaminants by F and Sn co-doped TiO₂ photoelectrode, Chem. Eng. J. 344 (2018) 332–341.

[76] F. Liang, Y. Zhu, Enhancement of mineralization ability for phenol via synergetic effect of photoelectrocatalysis of g-C₃N₄ film, Appl. Catal. B-Environ. 180 (2016) 324–329.

[77] B.O. Orimolade, B.A. Koiki, G.M. Peleyeju, O.A. Arotiba, Visible light driven photoelectrocatalysis on a FTO/BiVO₄/BiOI anode for water treatment involving emerging pharmaceutical pollutants, Electrochim. Acta 307 (2019) 285–292.

[78] R. Daghrir, P. Drogui, D. Robert, Photoelectrocatalytic technologies for environmental applications, J. Photochem. Photobiol. A: Chem. 238 (2012) 41–52.

[79] M.O. Miranda, W.E. Cabral Cavalcanti, F.F. Barbosa, J. Antonio de Sousa, F. Ivan da Silva, S.B.C. Pergher, T.P. Braga, Photocatalytic degradation of ibuprofen using titanium oxide: insights into the mechanism and preferential attack of radicals, RSC Adv. 11 (2021) 27720–27733.

[80] Z. Wang, V. Srivastava, I. Ambat, Z. Safaei, M. Sillanpää, Degradation of Ibuprofen by UV-LED/catalytic advanced oxidation process, J. Water Process Eng. 31 (2019), 100808.

[81] X. Zhao, J. Qu, H. Liu, Z. Qiang, R. Liu, C. Hu, Photoelectrochemical degradation of anti-inflammatory pharmaceuticals at Bi₂MoO₆–boron-doped diamond hybrid electrode under visible light irradiation, Appl. Catal. B: Environ. 91 (2009) 539–545.

[82] M.V.B. Zanoni, J.J. Sene, H. Selcuk, M.A. Anderson, Photoelectrocatalytic Production of Active Chlorine on Nanocrystalline Titanium Dioxide Thin-Film Electrodes, Environ. Sci. Technol. 38 (2004) 3203–3208.

[83] S.J. De-Nasri, S. Nagarajan, P.K.J. Robertson, V.V. Ranade, Quantification of hydroxyl radicals in photocatalysis and acoustic cavitation: Utility of coumarin as a chemical probe, Chem. Eng. J. 420 (2021), 127560.

[84] K. Hirano, T. Kobayashi, Coumarin fluorometry to quantitatively detectable OH radicals in ultrasound aqueous medium, Ultrason Sonochem. 30 (2016) 18–27.

[85] J. Zhang, Y. Nosaka, Quantitative Detection of OH Radicals for Investigating the Reaction Mechanism of Various Visible-Light TiO₂ Photocatalysts in Aqueous Suspension, J. Phys. Chem. C. 117 (2013) 1383–1391.

[86] S. Nagarajan, N.C. Skillen, F. Fina, G. Zhang, C. Randorn, L.A. Lawton, J.T. S. Irvine, P.K.J. Robertson, Comparative assessment of visible light and UV active photocatalysts by hydroxyl radical quantification, J. Photochem. Photobiol. A: Chem. 334 (2017) 13–19.

[87] J. Zhang, Y. Nosaka, Generation of OH radicals and oxidation mechanism in photocatalysis of WO₃ and BiVO₄ powders, J. Photochem. Photobiol. A: Chem. 303- 304 (2015) 53–58.

[88] C. Yang, F. Li, T. Li, A one-step ionic liquid-assisted ultrasonic method for the preparation of BiOCl/m-BiVO₄ heterojunctions with enhanced visible light photocatalytic activity, CrystEngComm 17 (2015) 7676–7683.

[89] X. Xu, Y. Sun, Z. Fan, D. Zhao, S. Xiong, B. Zhang, S. Zhou, G. Liu, Mechanisms for·O2- and·OH Production on Flowerlike BiVO₄ Photocatalysis Based on Electron Spin Resonance, Front. Chem. 6 (2018).

[90] I. Papagiannis, P. Stathi, T. Deligiannakis, A. Keramidas, P. Lianos, Photoelectrocatalytic production of hydrogen peroxide using a photo(catalytic) fuel cell, J. Photochem. Photobiol. A: Chem. 389 (2020), 112210.

[91] S. Garcia-Segura, E. Brillas, Applied photoelectrocatalysis on the degradation of organic pollutants in wastewaters, J. Photochem. Photobiol. C: Photochem. Rev. 31 (2017) 1–35.

[92] J. Liu, Y. Zou, B. Jin, K. Zhang, J.H. Park, Hydrogen Peroxide Production from Solar Water Oxidation, ACS Energy Lett. 4 (2019) 3018–3027.

[93] X. Xue, Y. Wang, Z. Pan, K. Sayama, Electrochemical and Photoelectrochemical Water Oxidation for Hydrogen Peroxide Production, Angew. Chem. Int. Ed. 60 (2021) 10469–10480.

[94] K. Fuku, K. Sayama, Efficient oxidative hydrogen peroxide production and accumulation in photoelectrochemical water splitting using a tungsten trioxide/bismuth vanadate photoanode, Chem. Commun. 52 (2016) 5406–5409.

[95] K. Zhang, J. Liu, L. Wang, B. Jin, X. Yang, S. Zhang, J.H. Park, Near-Complete Suppression of Oxygen Evolution for Photoelectrochemical H₂O Oxidative H₂O₂ Synthesis, J. Am. Chem. Soc. 142 (2020) 8641–8648.

[96] N. Farhadi, T. Tabatabaie, B. Ramavandi, F. Amiri, Ibuprofen elimination from water and wastewater using sonication/ultraviolet/hydrogen peroxide/zeolite-titanate photocatalyst system, Environ. Res. 198 (2021), 111260.

[97] S. Zhang, I. Ahmet, S.-H. Kim, O. Kasian, A.M. Mingers, P. Schnell, M. Kölbach, J. Lim, A. Fischer, K.J.J. Mayrhofer, S. Cherevko, B. Gault, R. van de Krol, C. Scheu, Different Photostability of BiVO₄ in Near-pH-Neutral Electrolytes, ACS Appl. Energy Mater. 3 (2020) 9523–9527.

[98] F.M. Toma, J.K. Cooper, V. Kunzelmann, M.T. McDowell, J. Yu, D.M. Larson, N. J. Borys, C. Abelyan, J.W. Beeman, K.M. Yu, J. Yang, L. Chen, M.R. Shaner, J. Spurgeon, F.A. Houle, K.A. Persson, I.D. Sharp, Mechanistic insights into chemical and photochemical transformations of bismuth vanadate photoanodes, Nat. Commun. 7 (2016) 12012.

[99] T.W. Kim, K.-S. Choi, Nanoporous BiVO₄ Photoanodes with Dual-Layer Oxygen Evolution Catalysts for Solar Water Splitting, Science 343 (2014) 990–994.

[100] F.F. Abdi, L. Han, A.H.M. Smets, M. Zeman, B. Dam, R. van de Krol, Efficient solar water splitting by enhanced charge separation in a bismuth vanadate-silicon tandem photoelectrode, Nat. Commun. 4 (2013) 2195.

[101] D.K. Lee, K.-S. Choi, Enhancing long-term photostability of BiVO₄ photoanodes for solar water splitting by tuning electrolyte composition, Nat. Energy 3 (2018) 53–60.

[102] J.H. Baek, T.M. Gill, H. Abroshan, S. Park, X. Shi, J. Nørskov, H.S. Jung, S. Siahrostami, X. Zheng, Selective and Efficient Gd-Doped BiVO$_4$ Photoanode for Two-Electron Water Oxidation to H$_2$O$_2$, ACS Energy Lett. 4 (2019) 720–728.

[103] F. Méndez-Arriaga, S. Esplugas, J. Giménez, Degradation of the emerging contaminant ibuprofen in water by photo-Fenton, Water Res. 44 (2010) 589–595.

[104] C. Regmi, Y.K. Kshetri, T.-H. Kim, R.P. Pandey, S.W. Lee, Visible-light-induced Fe-doped BiVO$_4$ photocatalyst for contaminated water treatment, Mol. Catal. 432 (2017) 220–231.

[105] N. Jallouli, L.M. Pastrana-Martínez, A.R. Ribeiro, N.F.F. Moreira, J.L. Faria, O. Hentati, A.M.T. Silva, M. Ksibi, Heterogeneous photocatalytic degradation of ibuprofen in ultrapure water, municipal and pharmaceutical industry wastewaters using a TiO$_2$/UV-LED system, Chem. Eng. J. 334 (2018) 976–984.

[106] F. Méndez-Arriaga, R.A. Torres-Palma, C. Pétrier, S. Esplugas, J. Gimenez, C. Pulgarin, Ultrasonic treatment of water contaminated with ibuprofen, Water Res. 42 (2008) 4243–4248.

[107] Y. Xiang, J. Fang, C. Shang, Kinetics and pathways of ibuprofen degradation by the UV/chlorine advanced oxidation process, Water Res. 90 (2016) 301–308.

[108] X. Li, Y. Wang, S. Yuan, Z. Li, B. Wang, J. Huang, S. Deng, G. Yu, Degradation of the anti-inflammatory drug ibuprofen by electro-peroxone process, Water Res. 63 (2014) 81–93.